Korean J. Chem. Eng., 34(2), 495-499 (2017)
DOI: 10.1007/s11814-016-0283-3

pISSN: 0256-1115
eISSN: 1975-7220

Polyol-mediated synthesis of ZnO nanoparticle-assembled hollow spheres/nanorods and their photoanode performances

Soon Wook Kim*, Tri Khoa Nguyen*, Doan Van Thuan*, Dinh Khoi Dang, Seung Hyun Hur**, Eui Jung Kim**,†, and Sung Hong Hahn***

*Department of Physics and Energy Harvest-storage Research Center, University of Ulsan, Ulsan 44610, Korea
**Department of Chemical Engineering, University of Ulsan, Ulsan 44610, Korea
(*Received 5 July 2016 • accepted 11 October 2016*)

Abstract−ZnO nanoparticle-assembled hollow spheres (raspberry-like) and elliptical nanorods (rice-like) were synthesized via a facile polyol process. Employing ethylene glycol as a polyol led to a ZnO nanoparticle-assembled hollow sphere structure, while diethylene glycol resulted in an elliptical nanorod structure. The ZnO hollow spheres had a higher Brunauer-Emmett-Teller (BET) surface area, better dye adsorption, more incident light trapping, and lower defect density than the ZnO elliptical nanorods. The ZnO hollow sphere-based dye-sensitized solar cells (DSSCs) exhibited a three-times higher current density than the ZnO elliptical nanorod-based DSSCs.

Keywords: ZnO Hollow Spheres, ZnO Elliptical Nanorods, Polyol Process, Dye-sensitized Solar Cells

INTRODUCTION

Zinc oxide (ZnO) is a multifunctional semiconductor with a wide band gap of 3.34 eV, a high exciton binding energy of 60 meV, and a fast electron mobility of 115-155 $cm^2/(V \cdot s)$. Due to its unique properties, ZnO finds many applications in areas such as photoelectronics, photovoltaics, and photocatalysis [1-5]. In particular, ZnO is regarded as a promising photoanode material for dye-sensitized solar cells (DSSCs). It is known that the microstructure of the ZnO photoanode in DSSCs strongly affects device performance. A high surface area for effective dye loading, light scattering for good light harvesting ability, densely packed structure for effective electron transport, and less charge recombination are required for enhanced photoanode performance [6].

TiO_2 is known as an excellent photoanode material for the DSSCs. Other oxide materials such as WO_3, SnO_2, Al_2O_3 and ZnO have been investigated to substitute for TiO_2 [7-9]. Among them, ZnO has attracted considerable interest because of its relatively fast electron mobility of 115-155 $cm^2V^{-1}s^{-1}$ [10] and various morphologies including nanorods [11] nanoflowers [12], hollow spheres [13] and core-shell nanoparticles [14]. Wet chemical techniques have been widely employed to synthesize ZnO nanostructures because of their low cost synthesis, low processing temperature, and good reproducibility. Shi et al. obtained ZnO hierarchical flowers through ultrasonic-assisted precipitation [15]. ZnO hierarchical flowers were composed of interlaced nanosheets and their porous and ultrathin structure has the benefits of light capturing and electron transporting ability in DSSCs. Jana et al. synthesized ZnO rods with different aspect ratios by using a two-stage solution process at 80 °C for 6 h and compared their photoanode performance in DSSCs [16]. ZnO rods with a lowest aspect ratio had a high surface area of 42 m^2/g and exhibited a solar conversion efficiency of 1.38%. Memarian et al. fabricated hierarchically assembled ZnO nanocrystallites and investigated the effects of the annealing temperature of the photoanodes, dye loading time, and buffer layer in the DSSCs [17]. Annealing the ZnO photoanode with a buffer layer at 450 °C greatly improved the photoconversion efficiency. Hu et al. synthesized ZnO nanocrystals with high purity, homogeneity, and tunable particle morphology by using a microwave-polyol process [18].

In this study, we synthesized ZnO nanoparticle-assembled hollow spheres (ZnO HSs) and ZnO nanorods (ZnO NRs) by a polyol process. The morphology, photoluminescence, surface area, and photo-response of the prepared ZnO nanostructures were compared. The ZnO HSs and NRs had quite different dye loading, BET surface area, diffuse reflectance, and defect density properties. The ZnO HSs exhibited higher photoanode performance than the ZnO NRs.

MATERIALS AND METHODS

1. Synthesis of ZnO Hollow Spheres and Nanorods

0.5 mL of 1 M zinc acetate dehydrate ($Zn(CH_3COO)_2 \cdot 2H_2O$, Yakuri) was mixed with 20 mL of ethylene glycol ($C_2H_6O_2$, Daejung) to synthesize ZnO HSs and with 20 mL of diethylene glycol ($C_4H_{10}O_3$, Yakuri) to synthesize ZnO NRs. The mixture was contained in a 50 mL glass bottle and stirred at 180 °C for 20 min. After cooling to room temperature, whitish precipitates were separated by centrifugation and then cleansed with water and ethanol several times. The cleansed powders were dried at 60 °C for 24 h.

2. Fabrication of Dye-sensitized Solar Cells

0.02 g of ZnO powder was dispersed in 1 mL of water using sonication for 10 s and then 0.04 mL of the ZnO solution was dropped onto an FTO substrate with an active area of 0.28 cm^2. The ZnO photoanode layer was dried at room temperature for 24 h. The as-

†To whom correspondence should be addressed.
E-mail: ejkim@ulsan.ac.kr

prepared ZnO photoanode was immersed in 0.3 mM N719 dye (di-tetrabutylammonium cis-bis (isothiocyanato) bis (2,2′-bipyridyl-4,4′-dicarboxylato) ruthenium(II), Sigma Aldrich) in ethanol and sensitized at 30 °C for 2 h. The counter electrode was fabricated by spray coating 5 mL of an H_2PtCl_6 solution (5 mM in isopropanol) on an FTO substrate followed by annealing at 380 °C for 20 min. The photoanode and counter electrode substrates were assembled using a hot-melt sealing film (100 μm) at 100 °C for 15 min. Then, iodine/tri-iodine electrolyte (Solaronix, AN-50) was injected into the interspace between the photoanode and counter electrode.

3. Characterization

The morphologies of the samples were examined using a field emission scanning electron microscope (FE-SEM, JEOL JSM6500F) operated at 10 kV and a high resolution-scanning transmission electron microscope (HR-STEM, JOEL JEM-2200FS) operated at 200 keV. Crystal structure analysis of ZnO was performed by X-ray diffraction (XRD) with CuKα radiation. PL spectra were recorded at room temperature by exciting the samples with a 325 nm He-Cd laser (IK3301R-G, Kimmon Koha) at an output power of 30 mW. A monochromator (DM150i, Dongwoo Optron) was used to collect the photon emission. The diffuse reflectance and dye loading absorbance were measured by using a UV/Vis spectrophotometer (Cary 5000 and HP, UV-Vis 8453, respectively). The specific surface areas were determined from the Brunauer-Emmett-Teller (BET) method (ASAP-2420, Micromeritics Inst.). Photocurrents were recorded using a KEITHLEY 2420 source meter under AM 1.5G, 100 mW/cm^2 irradiation (Xenon lamp, LCS-100 solar simulator, Newport).

RESULTS AND DISCUSSION

1. Crystal Structure and Morphology

Fig. 1 shows the XRD patterns and SEM images of the synthe-

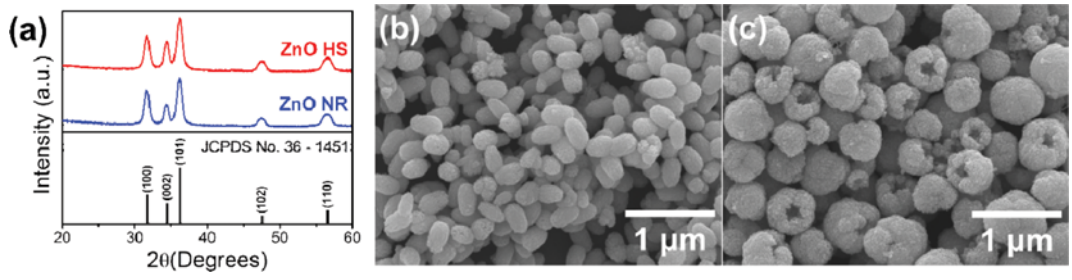

Fig. 1. (a) X-ray diffraction (XRD) patterns of the ZnO structures and surface scanning electron microscopy (SEM) images of (b) ZnO NRs and (c) ZnO HSs.

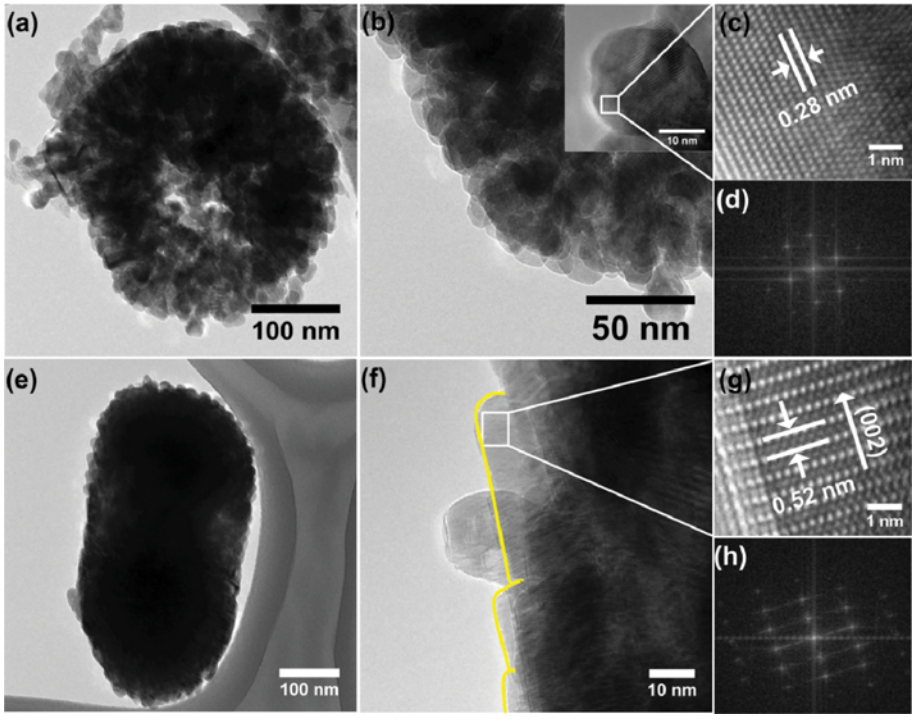

Fig. 2. Transmission electron microscopy (TEM) images and selected area electron diffraction (SAED) patterns of the (a)-(d) ZnO HSs and (e)-(h) ZnO NRs.

sized ZnO HSs and NRs. As can be seen in the XRD patterns of the ZnO nanostructures (Fig. 1(a)), (100), (002), and (101) peaks are present which are assigned to the wurtzite structure (JCPDS Card No. 36-1451). The XRD peak intensities of the ZnO HSs are similar to those of the ZnO NRs, demonstrating that their grain sizes are almost the same. The intensity ratios of the (100) and (002) peaks ($I_{(100)}/I_{(002)}$) of the ZnO HSs and NRs are 1.07 and 1.58, respectively. This indicates that the ZnO NRs have a longitudinal morphology compared to the ZnO HSs. As shown in the SEM images of the ZnO HSs and NRs (Figs. 1(b)-(c)), the ZnO HSs have a hollow sphere morphology with an average diameter of about 400 nm, while the ZnO NRs have an elliptical rod shape with an aspect ratio of about 0.55 (length of 365 nm and width of 200 nm).

The HR-TEM images and corresponding FFT patterns of the ZnO HSs and NRs are presented in Fig. 2. The HR-TEM images clearly reveal that the HS structure is composed of assembled 20 nm primitive nanoparticles, while the NR structure consists of tightly arranged primitive nanorods. The primitive nanoparticles have clear lattice fringes with an interplanar spacing of 0.28 nm, which corresponds to the {100} facets of hexagonal wurtzite ZnO. The primitive nanorods have lattice fringes with an interplanar spacing of 0.52 nm, which matches the (002) plane. The bright diffraction spots in the FFT patterns shown in Figs. 2(d) and 2(h) confirm the high crystallinity of the synthesized ZnO nanoparticles and nanorods.

2. Adsorption Ability

The BET method was employed to determine the specific surface areas of the ZnO nanostructures. The nitrogen adsorption-desorption isotherms for ZnO are shown in Figs. 3(a)-(b). The BET surface area of the HS structure was found to be 30.67 m^2/g, which is significantly larger than that of the NR structure (8.58 m^2/g). The pore volumes of the ZnO HSs and NRs are 0.084 cm^3/g (pore size of 10.97 nm) and 0.036 cm^3/g (pore size of 16.67 nm), respectively. The ZnO HSs have a larger surface area, which may attract more dye molecules and strongly affect the photocurrent of ZnO-based DSSCs. The dye loading was determined from the UV-Vis absorption spectra after complete removal of the dye N719 molecules from the ZnO surface using 0.1 M NaOH, as shown in

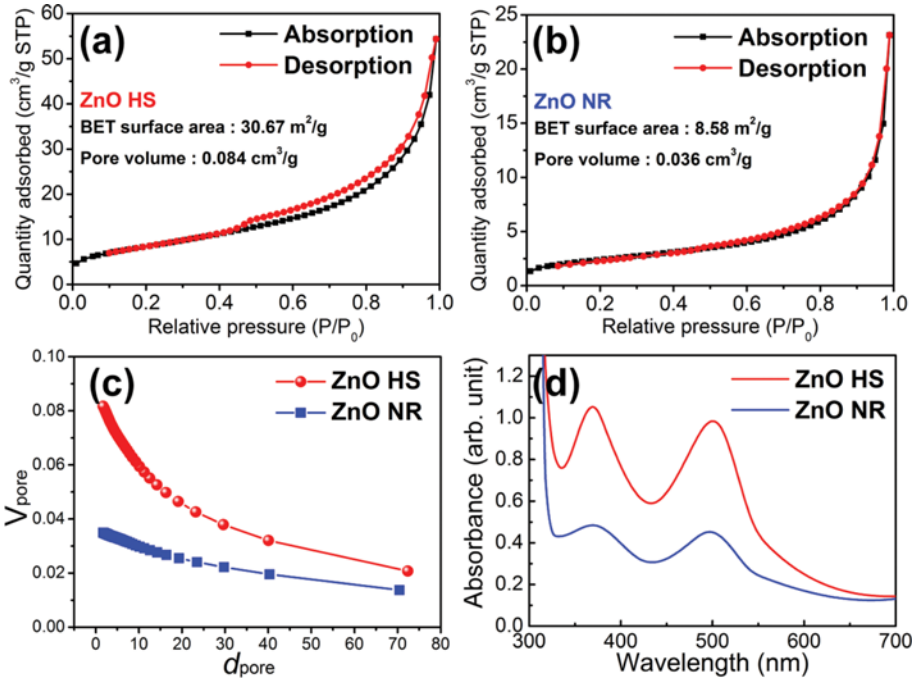

Fig. 3. Nitrogen adsorption-desorption isotherms of the (a) ZnO NRs and (b) ZnO HSs. (c) Pore volumes of the samples. (d) UV/Vis absorption spectra of dye removed from the surface of ZnO structures using a 0.1 M NaOH aqueous solution.

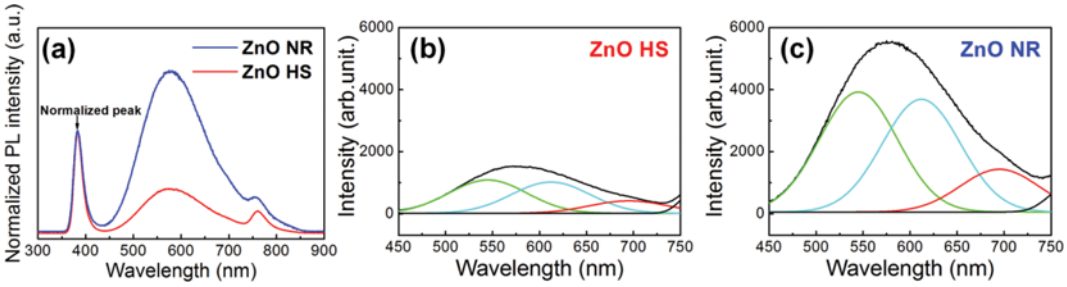

Fig. 4. (a) Normalized PL spectra and (b), (c) Gaussian fit defect peaks of the ZnO HSs and NRs.

Fig. 3(d) [19]. The absorption peak centers at 368 and 502 nm are due to the metal-to-ligand charge transfer (MLCT) of dye N719. The ZnO HSs exhibit better dye adsorption than the NR structure, which is demonstrated by the higher absorption peak intensity of desorbed dye. This results from the larger pore volume and BET surface area of the HS structure compared to the NR structure.

3. Photoluminescence Properties

Fig. 4(a) shows the photoluminescence (PL) spectra of the ZnO HSs and NRs, which provide information of electron recombination at the ZnO photoanode interface in the DSSCs. A band peak and a broad green defect emission appear at 384 nm and 575 nm, respectively, in Fig. 4(a). The intensity ratio of the green emission peak to the band peak was found to be 0.63 for the HS structure and 2.32 for the NR structure, indicating that the samples have different defect densities. To further investigate the green emission, the green emission peaks of the ZnO HSs and NRs were fit by Gaussian functions, as shown in Figs. 4(b) and 4(c), respectively. The green emission peak is deconvoluted into three Gaussian functions centered at approximately 545 nm (2.27 eV), 612 nm (2.02 eV), and 695 nm (1.78 eV), which are associated with defects such as zinc and oxygen vacancies. These defects and vacancies in ZnO reduce the device performance by trapping photo-generated electrons [20, 21]. The length of the glycol chain affects the particle size and the amount of defects in the resulting nanostructure. The chain length of EG is shorter than that of DEG, resulting in the formation of spherical particles. The extended morphology of the ZnO NRs incurs the creation of surface defects and exciton quenching [22]. Accordingly, the ZnO HSs with a low defect emission transports more photogenerated electrons from the dye to FTO electrode than the ZnO NRs.

4. Diffuse Reflectance

The UV-Vis diffuse reflectance spectra of the ZnO nanostructures are illustrated in Fig. 5. The ZnO HSs possess a lower diffuse reflection in the wavelength range of 400 to 800 nm than the ZnO NRs before dye adsorption, as shown in Fig. 5(a). A lower diffuse reflectance results from the increased light-harvesting efficiency due to the higher light scattering effect, improving the photocurrent density (J_{SC}) [23,24]. The low diffuse reflectance of the HS structure compared to the NR structure may originate from the rough surface of the HS structure, which enhances light trapping. We also obtained the diffuse reflectance spectra of the N719 dye adsorbed-ZnO surface to investigate the effect of light trapping in the photoanode of the DSSCs [25,26]. As shown in Fig. 5(b), the dye adsorbed-ZnO HS shows a lower diffuse reflectance than the ZnO NRs. More dye molecules can be adsorbed on both the external and internal surfaces of the ZnO HSs, leading to an improvement of the optical absorption due to the increased interaction of photons with dye molecules. Accordingly, the ZnO HSs are more effective in light harvesting than the ZnO NRs.

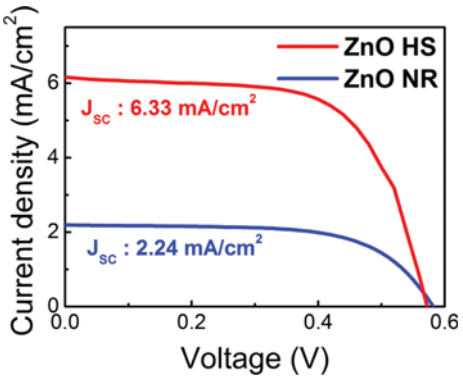

Fig. 6. Current-voltage curves of the ZnO structures.

5. Photocurrent Response

Fig. 6 shows the current-voltage curves for the ZnO HS and NR-based DSSCs. The ZnO HSs have a photocurrent density (J_{SC}) of 6.33 mA/cm^2 at 0 V, which is higher than that of the ZnO NRs (2.24 mA/cm^2). The open circuit voltage (V_{OC}) and fill-factor (FF) are 6.33 V and 0.64, respectively, in the case of the ZnO HSs, while they are 0.58 V and 0.64 for the ZnO NRs, respectively. As a result, the photoconversion efficiency of the ZnO HSs (2.31%) is better than that of the ZnO NRs (0.83%). A high photocurrent density of the ZnO HSs compared to the ZnO NRs is mainly due to two factors: (i) the injection of more electrons from the dye to the ZnO HS photoanode due to its larger BET surface area, resulting in the adsorption of more dye molecules, and (ii) the relatively long lifetime of electrons as a result of the low recombination rate of photogenerated electrons and holes.

CONCLUSIONS

We synthesized ZnO nanoparticle-assembled hollow sphere (HS) and ZnO elliptical nanorod (NR) structures via a facile polyol-

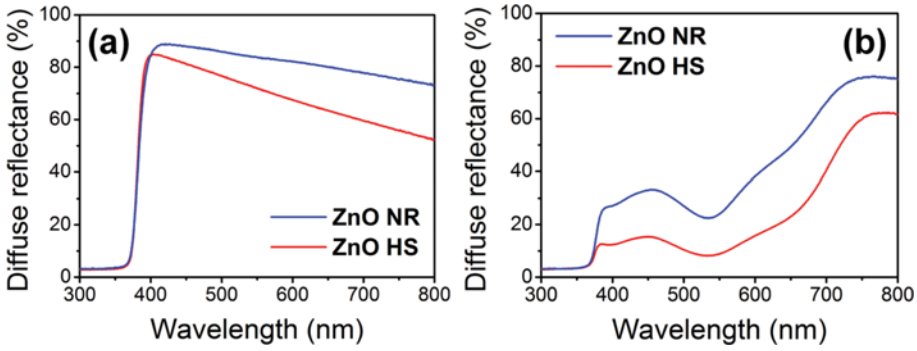

Fig. 5. Diffuse reflectance spectra of ZnO structures (a) before and (b) after dye adsorption.

mediated solvothermal process. The BET surface area of the ZnO HSs was three-times larger than that of the ZnO NRs. More dye molecules were adsorbed on the surface of the ZnO HSs compared to the ZnO NRs. In addition, the ZnO HSs absorbed more light by gathering incident light into the hollow sphere. Lower crystalline defects in the HS structure led to better electron transport at the ZnO-dye interface in comparison with the NR structure. The ZnO HSs showed a short-circuit current density of 6.33 mA/cm^2, which is higher than that of the ZnO NRs (2.24 mA/cm^2).

REFERENCES

1. J. A. Anta, E. Guillen and R. Tena-Zaeta, *J. Phys. Chem. C*, **116**, 11413 (2012).
2. S. H. K. Park, C. S. Hwang, M. Ryu, S. Yang, C. Byun, J. Shin, J. I. Lee, K. Lee, M. S. Oh and S. Im, *Adv. Mater.*, **21**, 678 (2009).
3. P. I. Reyes, C. J. Ku, Z. Duan, Y. Xu, E. Garfunkel and Y. Lu, *Appl. Phys. Lett.*, **101**, 031118 (2012).
4. M. Farzadkia, K. Rahmani, M. Gholami, A. Esrafili, A. Rahmani and H. Rahmani, *Korean J. Chem. Eng.*, **31**, 2014 (2014).
5. E. D. Sherly, J. J. Vijaya, L. J. Kennedy, A. Meenakshisundaram and M. Lavanya, *Korean J. Chem. Eng.*, **33**, 1431 (2016).
6. G. S. Selopal, N. Memarian, R. Milan, I. Concina and G. Sberveglieri, *ACS Appl. Mater. Interfaces*, **6**, 11236 (2014).
7. C.-L. Wang, J.-Y. Liao, Y. Zhao and A. Manthiram, *Chem. Commun.*, **51**, 2848 (2015).
8. H. Zheng, Y. Tachibana and K. Kalantar-zadeh, *Langmuir*, **26**, 19148 (2010).
9. M. Law, L. E. Greene, A. Radenovic, T. Kuykendall, J. Liphardt and P. Yang, *J. Phys. Chem. B*, **110**, 22652 (2006).
10. T. P. Chou, Q. Zhang, G. E. Fryxell and G. Cao, *Adv. Mater.*, **19**, 2588 (2007).
11. P. P. Das, S. A. Agarkar, S. Mukhopadhyay, U. Manju, S. B. Ogale and P. S. Devi, *Inorg. Chem.*, **53**, 3961 (2014).
12. J. Xu, K. Fan, W. Shi, K. Li and T. Peng, *Sol. Energy*, **101**, 150 (2014).
13. R. Ramakrishnan, A. Aravind, S. J. Devaki, M. R. Varma and K. Mohan, *J. Phys. Chem. C*, **118**, 19529 (2014).
14. X. Chen, Z. Bai, X. Yan, H. Yuan, G. Zhang, P. Lin, Z. Zhang, Y. Liu and Y. Zhang, *Nanoscale*, **6**, 4691 (2014).
15. Y. Shi, C. Zhu, L. Wang, W. Li, C. Cheng, K. M. Ho, K. K. Fung and N. Wang, *J. Mater. Chem.*, **22**, 13097 (2012).
16. A. Jana, P. P. Das, S. A. Agarkar and P. S. Devi, *Sol. Energy*, **102**, 143 (2014).
17. N. Memarian, I. Concina, A. Braga, S. M. Rozati, A. Vomiero and G. Sberveglieri, *Angew. Chem. Int. Ed.*, **50**, 12321 (2011).
18. X. Hu, J. Gong, L. Zhang and J. C. Yu, *Adv. Mater.*, **20**, 4845 (2008).
19. V. Thavasia, V. Renugopalakrishnan, R. Jose and S. Ramakrishna, *Mater. Sci. Eng. R*, **63**, 81 (2009).
20. N. T. Khoa, S. W. Kim, D. H. Yoo, S. Cho, E. J. Kim and S. H. Hahn, *ACS Appl. Mater. Interfaces*, **7**, 3524 (2015).
21. D. Barpuzary, A. S. Patra, J. V. Vaghasiya, B. G. Solanki, S. S. Soni and M. Qureshi, *ACS Appl. Mater. Interfaces*, **6**, 12629 (2014).
22. A. Dakhlaoui, M. Jendoubi, L. S. Smiri, A. Kanaev and N. Jouini, *J. Cryst. Growth*, **311**, 3989 (2009).
23. S. H. Hwang, D. H. Shin, J. Yun, C. Kim, M. Choi and J. Jang, *Chem. Eur. J.*, **20**, 4439 (2014).
24. Q. Zhang, D. Myers, J. Lan, S. A. Jenekhe and G. Cao, *Phys. Chem. Chem. Phys.*, **14**, 14982 (2012).
25. H. J. Koo, Y. J. Kim, Y. H. Lee, W. I. Lee, K. Kim and N. G. Park, *Adv. Mater.*, **20**, 195 (2008).
26. J. Yun, S. H. Hwang and J. Jang, *ACS Appl. Mater. Interfaces*, **7**, 2055 (2015).